Design and Operation of a Graphene-Based Plasmonic Nano-Antenna Array for Communication in the Terahertz Band

Arjun Singh, *Graduate Student Member, IEEE*, Michael Andrello III, *Student Member, IEEE*, Ngwe Thawdar, *Member, IEEE*, and Josep Miquel Jornet, *Member, IEEE*

***Abstract*— Terahertz (THz)-band (0.1 - 10 THz) communication is envisioned as a key wireless technology to satisfy the need for higher wireless data rates in denser networks. Several ongoing approaches are being considered to overcome the *grand challenge of the THz band*, i.e., the limited communication distance. Among others, the use of new 2D nanomaterials such as graphene to create novel plasmonic devices that operate directly in the THz range and can be densely packed has been proposed. This paper presents a novel THz plasmonic array architecture which leverages the properties of graphene to greatly simplify its design and operation. Each element of the plasmonic array is an independent front-end, consisting of an on-chip plasmonic source, modulator and antenna. The advantages of this array architecture over conventional array architectures are discussed. The trade-offs in the design of the front-end and the array are exhaustively studied in transmission. The ability to perform continuous dynamic beamforming is presented. A new tailored algorithm is developed for beamforming weight selection. Extensive numerical results are provided to demonstrate the functionality of the array for dynamic beamforming and increased power output.**

***Index Terms*— Terahertz communications, graphene plasmonics, array architecture, dynamic beamforming.**

I. Introduction

In an attempt to simultaneously provide faster wireless data rates to an ever increasing number of wirelessly connected devices, enabling wireless communications in the terahertz (THz) band has become a priority for several research groups worldwide [1]–[5]. The huge transmission bandwidth (from tens to hundreds of GHz) in the THz range (from 0.1 to 10 THz) can enable Terabit-per-second (Tbps) wireless links. However, the advantage of the THz band comes at the cost of very high propagation losses, which combined with the low transmission power of THz sources, severely limit the communication distance [6].

To overcome this challenge, several new device technologies have been proposed [7]. On the one hand, in an *electronic approach*, standard silicon complementary metal–oxide–semiconductor (CMOS), Silicon Germanium BiCMOS and III-V semiconductor, high electron mobility transistor (HEMT) and Schottky diode technologies are being pushed to their limits to reach the 1 THz mark [8]–[10]. On the other hand, in a *photonics approach*, quantum cascade lasers, optical down-conversion systems and photo-conductive antennas are being explored [11], [12].

In parallel to the development of higher power sources at true THz frequencies, the generated power needs to be efficiently radiated through directional antennas to increase the communication distance. Taking advantage of the very small wavelength of THz waves, compact directional horn and lens antennas, commercially available [13], [14] as well as other innovative antenna designs [15]–[17], all with gains of as much as 55 dB, are readily available. Such directional antennas are useful in static THz links (e.g., THz backhaul). However, in a mobile network, dynamic beamforming antenna arrays are required to dynamically steer the beam direction. For the time being, smart antenna arrays with programmable elements for dynamic beamforming have been demonstrated to work at up to 140 GHz [18], but existing antenna arrays at true THz frequencies do not support dynamic beamforming [19]–[21].

The challenges in reaching true THz frequencies and exploiting the available bandwidth motivate the exploration of new, alternative technologies. The use of graphene-based plasmonic devices which intrinsically operate in the THz range is one such promising alternative. Graphene is a two-dimensional carbon material that has excellent electrical conductivity, making it very well suited for propagating extremely-high-frequency electrical signals [22]. Moreover, graphene supports the propagation of highly tunable Surface Plasmon Polariton (SPP) waves directly at THz frequencies [23]. SPP waves are highly confined electromagnetic (EM) waves generated at the interface of a conductor and dielectric, with wavelengths as much as several orders of magnitude smaller than those of free-space EM waves at the same frequency. The highly confined wavelength of SPP waves and intrinsic tunability of graphene

Manuscript received October 1, 2019; revised January 15, 2020; accepted February 17, 2020. Date of publication June 8, 2020; date of current version August 28, 2020. Northeastern University acknowledges the U.S. Government's support in the publication of this article. This material is based upon work funded by AFRL, under AFRL Grant No. FA8750-20-1-0200. Any opinions, findings, and conclusions or recommendations expressed in this material are those of the author(s) and do not necessarily reflect the views of AFRL. Approved for Public Release; Distribution Unlimited: 88ABW-2020-0725. *(Corresponding author: Arjun Singh.)*

Arjun Singh and Josep Miquel Jornet are with the Department of Electrical and Computer Engineering, Northeastern University, Boston, MA 02120 USA (e-mail: singh.arj@northeastern.edu).

Michael Andrello III is with the Department of Electrical Engineering, University at Buffalo-The State University of New York, Buffalo, NY 14260 USA, and also with the U.S. Air Force Research Laboratory, Rome, NY 13441 USA.

Ngwe Thawdar is with the U.S. Air Force Research Laboratory, Rome, NY 13441 USA.

Color versions of one or more of the figures in this article are available online at http://ieeexplore.ieee.org.

Digital Object Identifier 10.1109/JSAC.2020.3000881

allow the development of novel graphene based plasmonic devices for signal generation & detection [24], [25], modulation & demodulation [26]–[28], and radiation [29], [30], which operate at true THz frequencies. Nonetheless, the limitation on power output of a single device and, therefore, on the possible communication distance, remains. This motivates the development of innovative array architectures [31], [32].

In this paper, we propose a new beamforming antenna array architecture for THz communications, which leverages the unique properties of graphene. More specifically, in our proposed architecture, every element is a complete THz front-end and consists of an on-chip plasmonic THz signal source, an on-chip plasmonic phase modulator and controller, and an on-chip plasmonic nano-antenna. The tunability of graphene is leveraged to dynamically change the amplitude and phase for application of beamforming weights at each element. In light of the beamforming capabilities demonstrated and, in particular, the interdependence of amplitude and phase selection, we propose a new tailored weight selection algorithm. Our results show that the proposed architecture can be used to design highly dense antenna arrays that can provide complete (i.e., simultaneous phase and amplitude) beamforming control and potentially outperform conventional array architectures.

The remainder of the paper is organized as follows. In Sec. II, we review the state of the art in THz antenna array and graphene plasmonics technology and motivate our approach. In Sec. III, we describe our proposed architecture, including its building blocks and compare it to the conventional antenna array architectures designed at lower frequencies. In Sec. IV, we focus on the design of the single front-end, whereas their control and integration in arrays is presented in Sec. V. In Sec. VI, we numerically study the trade-offs and evaluate the beamforming performance of our proposed array, through Finite Difference Frequency Domain (FDFD) full wave numerical simulations. We discuss the technical challenges and opportunities in realizing our array architecture in Sec. VII. We conclude our paper in Sec. VIII.

II. Related Works

There are several efforts aimed at the development of THz devices to explore the THz band and realize ultra high speed communication links.

A. THz Signal Sources

There are several approaches to generate THz signals. For a complete review of the field, we refer the readers to [7]. Here, we briefly describe the options providing high-power THz signals. Within the EM spectrum, the THz band lies halfway between RF and optics. As a result, there are both electronic and photonic approaches to generate THz signals.

Following an *electronic approach*, in [8], frequency oscillators at 109 GHz are utilized to design a frequency-multiplied CMOS-based voltage controlled oscillator (VCO), generating signals between 219 - 231 GHz. The peak output power is 3 dBM, or $2\,\mathrm{mW}$. In [33], a first of its kind of power amplifier, utilizing an InP based high electron mobility transistor (HEMT), is demonstrated to provide up to $9\,\mathrm{dB}$ gain at 1.03 THz. A signal source at higher frequencies is presented in [9], where a Schottky diode based frequency multiplier is used to up-convert signals from a Ga/As based source to generate signals at 1.2 THz, with a power output of up to $2.5\,\mu\mathrm{W}$. In [10], on-chip power combining is utilized to generate THz signals at up to 1.6 THz, using a GaN based HEMT amplifier module and a frequency multiplier chain. The power output obtained at 1.6 THz is $0.7\,\mathrm{mW}$.

In the *photonic approach*, the highest power generated is through the use of quantum cascade lasers (QCLs). Such devices can provide up to several mWs of power at frequencies above 1 THz [34], but their performance quickly drops at room temperature [12].

B. THz Antennas and Antenna Arrays

In addition to increasing the generated power directly through newer sources, directional antennas can be utilized to increase the communication distance. Conventional directional antennas, such as horn, lens, and Cassegrain reflector antennas can be commercially found at frequencies of up to 1 THz [13], [14]. Moreover, taking advantage of the very small wavelength of THz signals, several innovative antenna designs have been proposed. For example, in [15], a wide-band compact integrated antenna at 400 GHz with a bandwidth from 325-500 GHz is designed with multiple sub-reflectors, and a gain of $30\,\mathrm{dB}$. In [16], a dielectric lens is used to focus the radiation from a leaky wave guide and an antenna resonant at 545 GHz with gain of up to $30\,\mathrm{dB}$ is demonstrated.

To further increase the gain compared to a single directional antenna, arrays have been designed and developed at the THz range. For example, in [19], a 2×2 array is designed through a resonant micro-strip cavity antenna and demonstrated to have a gain of $16\,\mathrm{dB}$ compared to a horn antenna at 0.85 THz. The designed array has a large bandwidth, but is not designed for dynamic beamforming. In [20], a silicon based lens antenna is designed, and integrated into an array. The array is demonstrated to work at 1.9 THz. The aperture efficiency of the array is shown to be 85%. In [21] a chessboard antenna array is presented that has a photonic source and a bow tie antenna element. The array is shown to be able to improve power efficiency and operate at up to 2 THz. However, the array does not have dynamic beamforming capability, since the design is primarily focused on increasing the power efficiency.

C. Graphene-Based Tunable THz Devices

The aforementioned devices and methods successfully increase the power efficiency at THz frequencies, but do not provide dynamic beamforming capability as required in a mobile network. Graphene is highly tunable and, thus, can be leveraged for implementing devices that assist dynamic beamforming. For example, this property is used in [35] in the design of a patch antenna resonant at 4.3 THz, capable of dynamic beam-tilting of up to 30° from broadside. The element is designed by stacking a graphene based meta-material in between the patch and substrate. The peak gain is $6.6\,\mathrm{dB}$ and the main-lobe direction is dependent on the graphene intrinsic properties. However, the lack of an analytical model

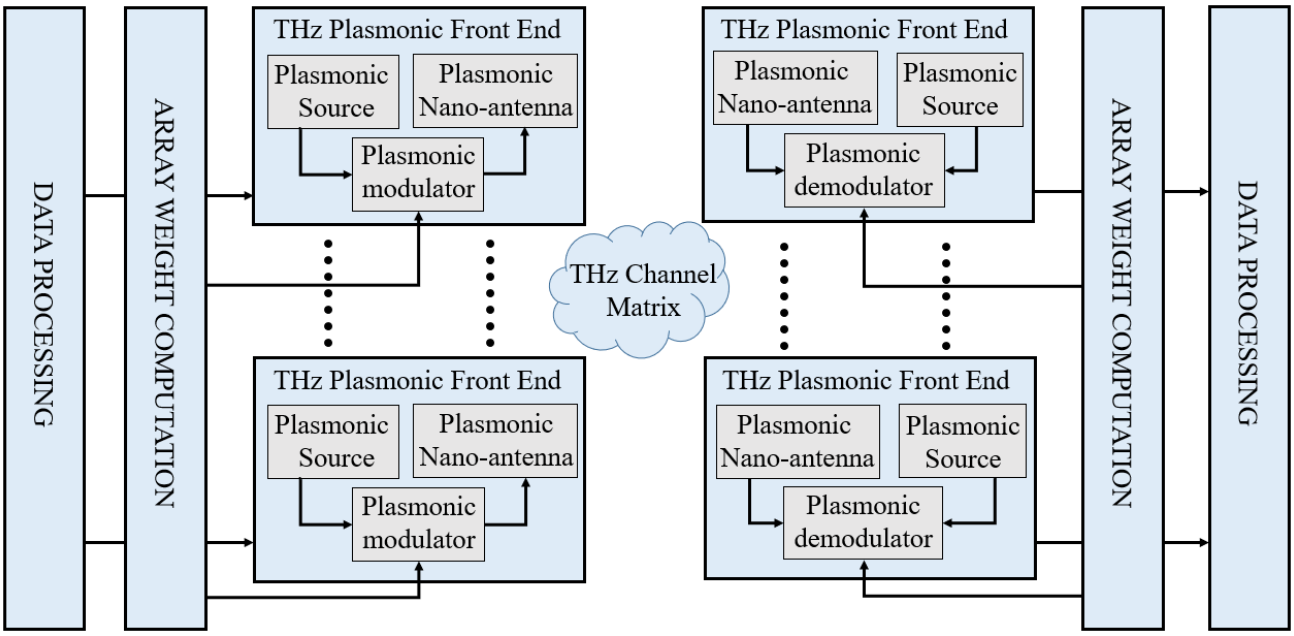

Fig. 1. Proposed graphene-based plasmonic nano-antenna array architecture.

to predict the actual tilting of the beam makes its extension to a dynamically beamforming antenna array impractical. In [36], a graphene based reconfigurable metasurface is designed for beamsteering capabilities. The proposed structure has independently controlled and integrated graphene based unit cells. The numerical results illustrate high tunability of the graphene cells, and a wide range (nearly 300°) of phase control. In [37], the compact size and low-loss features of graphene are considered in reducing the operating power and system complexity of conventional phased array architectures. Numerical analysis is performed to map the resultant phase of the elements of the array as graphene is tuned. In [38], the same method is used to propose an analog phase shifter with a graphene switch.

The efforts at developing THz-band communication devices have clearly achieved tremendous milestones. From the improvement of THz signal sources to the integration of antennas into arrays, the problem of limited communication distance is addressed in a non-trivial manner. The potential of exploiting the intrinsic properties of graphene for developing tunable THz devices is being explored as well. However, the establishment of a complete array architecture for true THz frequencies with dynamic beamforming is not fulfilled.

III. Graphene Based Plasmonic Nano-Antenna Array Architecture

Our proposed plasmonic array architecture is shown in Fig. 1. This architecture leverages the unique properties of graphene plasmonics to greatly simplify the array design. Each element in the proposed architecture is a complete THz front-end. At the transmitter, the plasmonic front-end consists of an on-chip plasmonic source, an on-chip plasmonic phase modulator and an on-chip plasmonic nano-antenna. The front-end at the receiver is designed similarly, but with a demodulator instead of the modulator. In this paper, we focus on the transmitter, though the proposed principles can be reciprocally applied to the receiver.

The source is designed to efficiently generate SPP waves directly at THz frequencies. First proposed in [24], the source is based on a HEMT built with a III-V semiconductor material and enhanced with graphene. The working principle is based on the Dyakonov-Shur instability [39], which predicts that a sub-micrometric resonant cavity with asymmetric boundary conditions can lead to THz emission. Compared to the previous works [40], [41], in our setup the THz emission is coupled to the graphene layer and utilized to launch SPP waves that propagate along the interface between graphene and air.

The generated SPP waves propagate on-chip towards the plasmonic modulator. First proposed in [27], the modulator consists of a graphene-based plasmonic waveguide. In this setup, by changing the Fermi energy of the graphene layer (i.e., the highest energy level occupied by electrons in graphene), for example, by means of electrostatic bias [42], the SPP wave propagation speed is modified. Given the finite length of the waveguide, a change in propagation speed leads to a change in phase at the output for a fixed observation time. Compared to other graphene-based modulators [26], the SPP waves propagate along the graphene layer and not through the graphene layer, leading to much stronger SPP wave modulation.

The SPP waves propagate along the modulator towards the plasmonic nano-antenna [29]. The antenna resembles a patch antenna with graphene as the active element and is able to convert the modulated SPP waves into free-space EM waves for emission. The working principle of the plasmonic nano-antenna is similar to that of a conventional patch antenna, i.e., it works as a broadside emitter on the basis of radiating slots. Additionally, by changing the Fermi energy of the graphene layer, the amplitude of the radiated fields can be controlled.

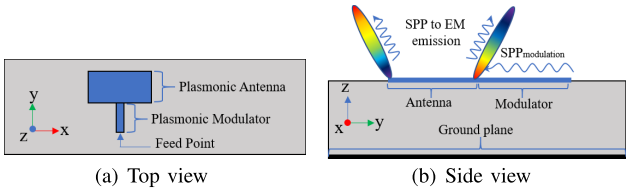

(a) Top view (b) Side view

Fig. 2. The working principle and design of the THz front end. The front end consists of a plasmonic source (represented here with the feed point), a plasmonic modulator and a plasmonic nano-antenna.: a) Top view; and b) Side view.

The proposed plasmonic array architecture differs from the conventional architectures in several ways. Each plasmonic front-end is powered by an independent source. The addition of more front-ends in an array does not simply improve the radiation direction efficiency, but the total output power is increased as well. The plasmonic modulator can directly manipulate the phase of SPP waves at THz frequencies without the need of any additional hardware. The nano-antenna has dimensions to resonate with the SPP wavelength λ_{spp}, and thus is much smaller than a regular patch antenna at the same frequency. The nano-antenna can also be tuned to provide amplitude control as needed. In this plasmonic array, the mutual coupling between the radiating elements depends on the SPP wavelength λ_{spp}, and not the free-space wavelength, λ_0. Thus, these front-ends can be packed into a very dense array. With no additional hardware, an independent power source per element, complete beamforming capability and an extremely small footprint, the plasmonic array fulfills the requirements of a complete dynamic beamforming system.

IV. Single Plasmonic Front-End Design

The front-end, illustrated in Fig. 2, forms the radiating element of the plasmonic array. Its individual design and performance directly impact the overall performance of the array. The design of the single front-end depends on the properties of SPP waves upon graphene. In this section, these properties are discussed in detail and the individual design of the components of the front-end are presented.

A. SPP Wave Propagation in Graphene

The properties of SPP waves on graphene are described by their complex wave vector k_{spp}. More specifically, the real part of the wave vector $\Re\{k_{\text{spp}}\}$ determines the plasmonic wavelength λ_{spp}, and the imaginary part of the wave vector $\Im\{k_{\text{spp}}\}$ determines the decay length D_L:

$$\lambda_{\text{spp}} = \frac{2\pi}{\Re\{k_{\text{spp}}\}} \text{ and} \tag{1}$$

$$D_L = \frac{1}{2\Im\{k_{\text{spp}}\}}. \tag{2}$$

The complex wave vector k_{spp} is found by solving the dispersion equation:

$$-i\frac{\sigma^g}{\omega\varepsilon_0} = \frac{\varepsilon_1 + \varepsilon_2 \coth(k_{\text{spp}}d)}{k_{\text{spp}}}, \tag{3}$$

where σ^g is the conductivity of graphene, ε_1 is the relative permittivity of the dielectric above graphene, ε_2 is the relative permittivity of the dielectric below graphene, and d is the separation between graphene and the metallic ground plane.

From (3), it is seen that the wave vector is related to the complex conductivity of graphene. This complex conductivity is obtained by following the Kubo formalism [43], [44] and can described by the following equations:

$$\sigma^g = \sigma^g_{\text{intra}} + \sigma^g_{\text{inter}}, \tag{4}$$

$$\sigma^g_{\text{intra}} = i\frac{2e^2}{\pi\hbar^2}\frac{k_BT}{\omega + i\tau^{-1}} \ln\left(2\cosh\left(\frac{E_F}{2k_BT}\right)\right), \tag{5}$$

$$\sigma^g_{\text{inter}} = \frac{e^2}{4\hbar}(H(\frac{\omega}{2}) + i\frac{4\omega}{\pi}\int_0^\infty \frac{G(\epsilon) - G(\omega/2)}{\omega^2 - 4\epsilon^2}d\epsilon, \tag{6}$$

and

$$G(a) = \frac{\sinh(\hbar a/k_BT)}{\cosh(E_F/k_BT) + \cosh(\hbar a/k_BT)}, \tag{7}$$

where ω is the angular frequency, $\hbar$ is the reduced Planck's constant, e is the electron charge, k_B is the Boltzmann constant, T is the temperature, E_F refers to the Fermi energy of the graphene sheet, and τ is the relaxation time of electrons in graphene. As shown in [45], at room temperature in graphene for THz frequencies, the main contribution is from the intra-band conductivity σ^g_{intra}.

From (3) and (4) it follows that the Fermi energy of graphene affects the conductivity, and in turn the wave vector. Therefore, the properties of SPP waves are tuned by varying the Fermi energy. The equations, however, are non-linear; therefore a numerical analysis is necessary to determine the exact relationship between the plasmonic wavelength and Fermi energy for a sheet of graphene, where all other variables are held constant.

B. Front-End Components

1) On-Chip Plasmonic THz Source: The design of the plasmonic source requires a multi-physics analysis aimed at self-consistently solving Maxwell's Equations and the Hydrodynamic Model Equations [25]. Given its complexity, its analysis is left outside the scope of this paper and, instead, we utilize a signal port to assess the performance of the modulator and nano-antenna.

2) On-Chip Plasmonic Phase Modulator: The physical length of the modulator is designed to minimize power dissipation while maintaining complete phase control. The total possible phase difference depends on both the physical length L of the modulator, as well as the range of Fermi energies considered applicable for tuning. This is seen in (8) below, where, for a modulator of considered physical length L, the phase difference Φ_{12} between two SPP waves with different plasmonic wavelengths λ_{spp_1} at Fermi energy E_{F_1}, and λ_{spp_2} at Fermi energy E_{F_2}, is derived to be

$$\Phi_{12} = 2\pi\frac{L}{\lambda_{\text{spp}_1}}\left(1 - \frac{\lambda_{\text{spp}_1}}{\lambda_{\text{spp}_2}}\right). \tag{8}$$

On the one hand, increasing the length of the modulator results in greater power dissipation along the modulator as

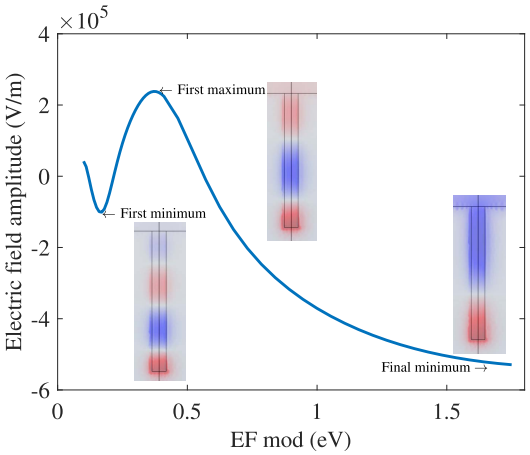

Fig. 3. Amplitude of the electric field at the output of the modulator as a function of the Fermi energy of the modulator EF_{mod}.

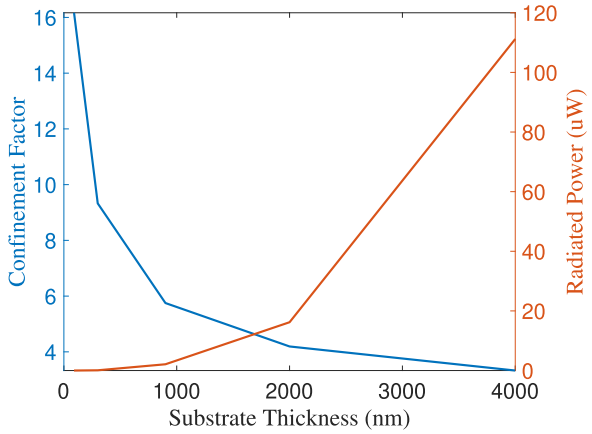

Fig. 4. The interdependence of confinement factor, substrate thickness and radiated power of the nano-antenna.

shown in Sec. VI, affecting the overall radiation efficiency of the front-end. On the other hand, reducing the length of the modulator clearly limits the achievable phase range (ideally, from 0 to 2π radians). To meet these objectives, the modulator is set with a physical length capable of incorporating an alteration of one complete plasmonic wavelength, λ_{spp}. In Fig. 3, the relation between the electric field amplitude at the output of the modulator is shown as a function of the Fermi energy of the modulator. The inner plots represent the electric field distribution on the modulator for three relevant values of the Fermi energy. It can be seen that, at different Fermi energies (all within the range between 0.1 and 1.75 eV), the corresponding output fields will exhibit a phase difference exceeding 2π.

3) On-Chip Plasmonic Nano-Antenna: The plasmonic nano-antenna is designed to be resonant at 1.025 THz, which corresponds to the first absorption-defined transmission window above 1 THz [4]. The working principle of the antenna is similar to the patch antenna, therefore the plasmonic antenna also has broadside emission. For resonance, the length of the antenna is half of the plasmonic wavelength λ_{spp} of the target frequency. The width of the antenna is determined through numerical evaluation for maximum radiation efficiency without significantly altering the expected broadside radiation pattern.

C. Design Trade-Offs

While the front-end elements have been discretely described, because both the modulator and the antenna share the same active element, i.e., a single graphene layer, they cannot be independently studied. The effect of the modulator on the radiation pattern of the combined front-end becomes non-negligible when the nano-antenna radiates inefficiently.

The SPP wave confinement factor, c_f, is one of the elements that plays a key role in the radiation efficiency of our system [46]. While there are several rigorous definitions of the confinement factor [47], an intuitive way to express it is:

$$c_f = \frac{\lambda_0}{\lambda_{\mathrm{spp}}}, \tag{9}$$

where λ_{spp} is the plasmonic wavelength and λ_0 is the free-space wavelength. From (3), λ_{spp} depends on the substrate thickness d. Using a thinner substrate increases the confinement factor, theoretically allowing the design of even smaller antennas and denser arrays. As observed in [48], when the antenna is designed at a very high confinement factor, its efficiency is decreased and the radiation pattern of the modulator becomes non-negligible. Comparing the structure of such a purposely designed inefficient front-end with that of [49], it is seen that the two structures exhibit certain symmetry. The properties of such a structure, similar to those of the design in [50], can be leveraged to design a front-end with a re-configurable radiation pattern, dependent on the Fermi energy of the modulator. However, the performance of the array in terms of power output as well as the range of beamsteering are compromised because, ultimately, this structure is not an efficient radiator.

To demonstrate the effects of the confinement factor on the radiation efficiency of the front-end, different resonant antennas are considered for the corresponding plasmonic wavelengths. The efficiency of each antenna is analysed using FDFD full-wave simulations with COMSOL Multi-physics. In Fig. 4, the relationship between confinement factor and the radiated power of the front-end is shown. It is clearly seen that as the confinement factor increases, the efficiency of the front-end drops drastically. This relation is also expected from the design constraints of patch antennas as given in [51]. The thickness of the substrate of a patch antenna is required to be between $0.003\lambda_0$ and $0.05\lambda_0$, for increased radiation efficiency. As explained in Sec. IV-B, the plasmonic antenna has a similar working principle as that of the patch antenna; the same constraints apply. As the confinement factor is increased, the thickness of the substrate is decreased and directly affects power output.

Considering this trade-off, the final dimensions of the front-end are summarized in Table I. The intrinsic properties of graphene, among them, the relaxation time, are modelled well within demonstrated values from latest fabrication methods, as in [52]–[54].

TABLE I
FRONT-END DIMENSIONS

Substrate thickness	2 µm
Substrate permittivity	$4\varepsilon_0$
Antenna resonant Fermi energy	1.25 eV
Antenna length ($0.5\lambda_{spp}$)	34.7 µm
Antenna width ($0.8\lambda_{spp}$)	52.05 µm
Modulator length	34.7 µm
Modulator width	3.47 µm
Graphene relaxation time	0.5 ps
Confinement factor	4.2

V. PLASMONIC ARRAY DESIGN AND CONTROL

The THz front-end developed in Sec. IV forms the active radiating element of the plasmonic array. The array is designed to provide support in establishing pencil thin beams through dynamic beamforming. In order to accomplish the task, the relationship between the elements of the array and the methods used to achieve it are discussed and presented here.

A. Spatial Arrangement of the Front-Ends

In traditional array design, to negate the effects of mutual coupling on array performance, at least one quarter free-space wavelength $\lambda_0/4$ spacing is kept between elements of the array [51]. In practice, the spacing is usually $\lambda_0/2$. A spacing greater than $\lambda_0/2$ results in the formation of undesired grating lobes [51]. However, in the case of plasmonic arrays, it is demonstrated in [55] that the effects of mutual coupling are negligible when the spacing between the elements exceeds the plasmonic wavelength, λ_{spp}. At the same time however, a reduced inter element spacing reduces the beamforming gain on the directivity, resulting in wider main-lobes [51]. Additionally, to achieve effective beamforming, the physical aperture of the array is required to be at minimum equal to λ_0 [51].

Therefore, keeping computational restrictions in mind, the plasmonic array is designed with a spatial geometry where each element is separated by a distance $\lambda_0/2$. This geometry achieves the optimal setup for the requirements discussed above. Thus, the performance of the array is not impacted by the negative effects of mutual coupling and, therefore, not discussed in the numerical analyses performed in Sec. VI. At the same time, a larger array aperture is analysed without stressing the computational limits of the FDFD solver.

B. Codebook Design

To steer a beam in the direction (θ_0, ϕ_0), the progressive phase delay, Φ_{rel}, between the elements of the array needs to be:

$$\Phi_{rel} = -k_0 d(sin\theta_0 cos\phi_0 + sin\theta_0 sin\phi_0), \tag{10}$$

where k_0 is the free-space wave vector and d is the separation between every element. Thus, dynamic beamforming requires phase control. Further, to control the amplitude of the beam (e.g., the relative power of the side-lobes), the amplitude of the signal at each element needs to be modified. The maximum output power of every element is governed by the source (given the lack of power amplifiers at THz frequency), hence amplitude control can only decrease the output power.

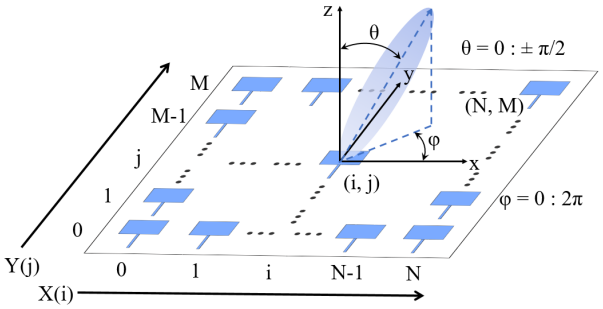

Fig. 5. Spatial geometry of the plasmonic array. The elevation angle θ_0 describes the deviation from the broadside direction, while the azimuth angle ϕ_0 describes the angle of the beam with the x-axis.

The planar plasmonic array is shown in Fig. 5. The elevation angle θ_0 and the azimuth angle ϕ_0 indicate the direction of the resultant beam. The array is considered to be in the xy plane, with the origin set in the leftmost corner of the array. Thus, the element at position $0, 0$ is the 0^{th} element, and every other element at the i, j position is required to be have a phase difference as from (10), for the desired (θ_0, ϕ_0). Implementing the desired phase difference and amplitude attenuation requires the definition of a codebook C composed of complex weights $W_{i,j}$, corresponding to the $\mathrm{i}, \mathrm{j}^{th}$ element. $W_{i,j}$ is of the form $Ae^{j\beta}$, where A represents the magnitude of the signal strength, and β represents the relative phase. The application of the derived codebook to the array results in beamforming. In the plasmonic array, the codebook is applied by varying the Fermi energy of the modulator, $EF_{\text{mod}_{i,j}}$, and the Fermi energy of the antenna $EF_{\text{ant}_{i,j}}$. Thus, the effective complex weight for a particular element, $W_{i,j}$, is mapped to a particular modulator and antenna Fermi energy of that element:

$$W_{\mathrm{i,j}} \mapsto EF_{\text{mod}_{i,j}}, EF_{\text{ant}_{i,j}}. \tag{11}$$

C. Independent Phase and Amplitude Control

One way to derive the codebook is to consider phase and amplitude control independently. The effective complex-valued weight $W_{i,j}$ is then formed as:

$$\Im\{W_{i,j}\} \mapsto f(EF_{\text{mod}_{i,j}}), \Re\{W_{i,j}\} \mapsto f(EF_{\text{ant}_{i,j}}). \tag{12}$$

As discussed in Sec. IV-B, phase control is achieved by the modulator. Consequently, the imaginary component of the weight that is affected in phase control is mapped to the Fermi energy of the modulator. Since phase control is relative, the effective weight for the element at the origin of the array is Ae^{j0}, and all other elements have an effective weight with phase delay as required to satisfy (10). The effective weight Ae^{j0} is naturally mapped to the Fermi energy of the modulator where the electric field amplitude is at the first minimum, obtained by following the relationship presented in Fig. 3. When the electric field amplitude crosses to the next minimum

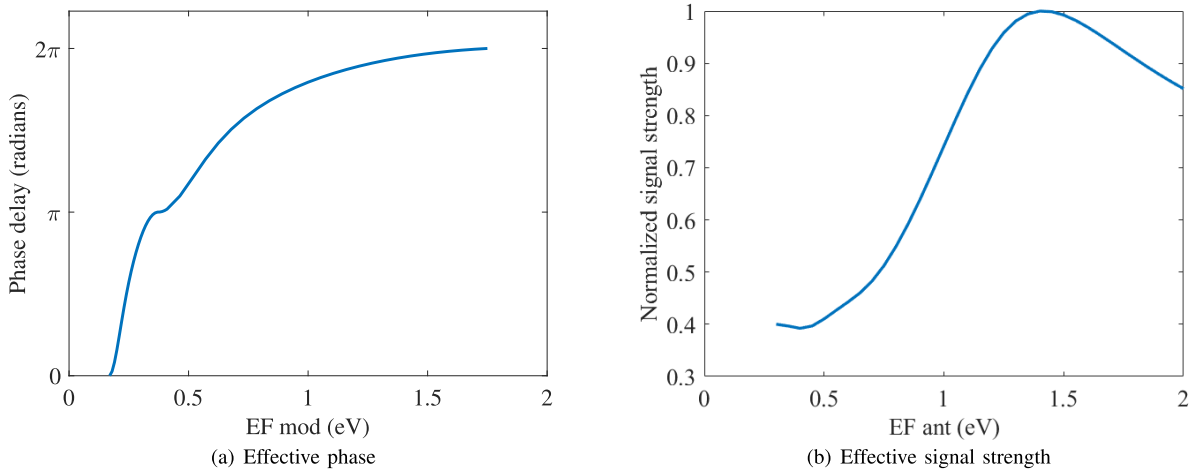

(a) Effective phase (b) Effective signal strength

Fig. 6. Demonstration of the tunability of the front-end: a) The relationship between the Fermi energy of the modulator EF_{mod} and the effective phase difference of the front-end; and b) The relationship between the Fermi energy of the antenna EF_{ant} and the effective signal strength of the front-end.

as the Fermi energy of the modulator is varied, a complete wavelength is traversed. Thus, the resultant phase change is of 2π radians. The particular Fermi energy of the modulator which corresponds to this point of the electric field amplitude then has the effective weight $Ae^{j2\pi}$.

Thus, any particular value for the Fermi energy of the modulator between these two values represents an effective weight between Ae^{j0} and $Ae^{j2\pi}$. As the Fermi energy is continuously varied, the achievable phase delay is also continuous, as opposed to common array architectures in which the phase can only be changed in discrete steps [56].

Following this approach, Fig. 6(a) presents the derived relation between the relative phase, β of the complex weight at the corresponding values of Fermi energy of the modulator EF_{mod}. It is seen that as EF_{mod} is varied from 0.17 - 1.75 eV, the effective weight varies from Ae^{j0} to $Ae^{j2\pi}$. Thus, 100% phase control is possible and the Fermi energy of the modulator can be set so as to achieve any required phase delay.

Similarly, as explained in Sec. IV-B, to enable amplitude control, the Fermi energy of the antenna is varied, affecting the radiation efficiency of the antenna. The antenna is designed for resonance, or peak performance, at a particular Fermi energy. Adjusting the Fermi energy of the antenna away from the resonant value makes amplitude control feasible.

In Fig. 6(b), the relation between the Fermi energy of the antenna and the corresponding normalized signal strength of the radiated signal is shown. It is seen that the normalized signal strength is maximum for the resonant Fermi energy value; increasing or decreasing the value of Fermi energy decreases the signal strength. Since the real part of the complex effective weight relates to the amplitude, the resonant Fermi energy value therefore corresponds to the effective weight S_0e^{j0}, where $S_0 = 1$. Any other value of the Fermi energy of the antenna represents an effective weight Se^{j0}, where $S \leq 1$. More specifically, as EF_{ant} is varied across 0.3 - 2 eV, the range of normalized signal strength varies from $0.38 \leq S \leq 1$. The total amplitude control possible is 62%.

As discussed in Sec. IV, the antenna is designed at a Fermi energy of 1.25 eV, thus the normalized signal strength is 1 at that value of Fermi energy of the antenna. Decreasing the Fermi energy of the antenna beyond 0.3 eV will continue to attenuate the signal strength, however the radiation pattern of the antenna is no longer broadside; the antenna effectively stops radiating below this value of Fermi energy.

The independent control of the front-end for both phase and amplitude control are thus directly dependent on the Fermi energy of the modulator and the antenna, respectively. Nevertheless, as discussed in Sec. IV-C, the modulator and the antenna cannot be either independently designed nor, consequently, operated. More specifically, varying the Fermi energy of the modulator effects the signal strength output of the front-end, and varying the Fermi energy of the antenna effects the phase delay of the front-end.

Fig 7 represents the joint relationship between the Fermi energies of the modulator and antenna on both the relative phase and normalized signal strength. More specifically, it is seen in Fig. 7(a), that for a constant value of the Fermi energy of the modulator EF_{mod}, the phase delay is effected as the Fermi energy of the antenna EF_{ant} is varied. Similarly, in Fig. 7(b), it is seen that for any particular Fermi energy of the antenna EF_{ant}, the signal strength is not constant as the Fermi energy of the modulator, EF_{mod} is varied. The negative impacts of this behavior on the beamforming capabilities of the array will be numerically studied in Sec. VI.

D. Joint Phase and Amplitude Control

While the consideration of independent phase and amplitude control exhibits its limitations, the incorporation of the joint relationship in determining effective weights presents itself as a challenge which increases the complexity of the beamforming algorithm. More specifically, the computation of the weight cannot be separated in two functions (12), but needs to be considered as a single function with two control variables:

$$W_{i,j} \mapsto f(EF_{\mathrm{mod}_{i,j}}, EF_{\mathrm{ant}_{i,j}}). \tag{13}$$

Unfortunately, there is no equation to quantify this joint effect. Instead, the weights need to be calculated through

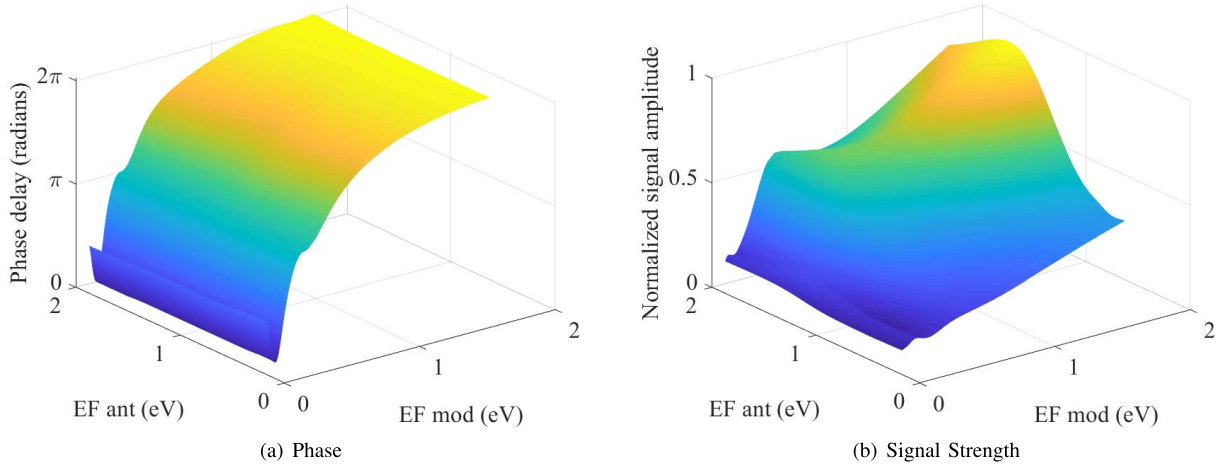

(a) Phase (b) Signal Strength

Fig. 7. Isometric view of the relationship between a) Phase delay at the front-end, and the Fermi energies of the modulator EF_{mod} and antenna EF_{ant}. b) Normalized signal strength at the front-end, and the Fermi energies of both the modulator EF_{mod} and antenna EF_{ant}.

exhaustive numerical simulations. For a given design, every combination of the Fermi energies of the modulator and antenna needs to be considered to derive the achievable complex weights. An algorithm can then be developed to retrieve the values of the Fermi energy of the modulator and the Fermi energy of the antenna corresponding to the effective weights needed for a given codebook, as required by array theory. The precision of the algorithm is determined by the richness of the data set; more data points increase the resolution.

The steps considered in such algorithm are shown below. The particular combination of $EF_{\mathrm{mod}}, EF_{\mathrm{ant}}$ which generates the desired effective weight, is searched for only once and these values are then stored for future use.

VI. Numerical Performance Analysis

In this section, we numerically investigate the performance of a single front-end and an array of the same in terms of phase and amplitude control and beamforming capabilities, respectively. Considering the computational intensity of the numerical simulations, we have restricted our analyses to a linear array. In the lack of mutual coupling between elements, a planar array can be analyzed as a combination of two linear arrays [51] and, thus, the results presented here are sufficient to prove the principles and demonstrate the capabilities of the proposed architecture.

A. Phase and Amplitude Control of a Single Front-End

All possible codebooks, C, attainable when we independently consider phase and amplitude control are derived from the individual phase and amplitude control relations presented in Fig. 6. The codebook so derived can then have the effective weights $W_{\mathrm{Independent}_{\mathrm{codebook}}}$, given by

$$W_{\mathrm{Independent}_{\mathrm{codebook}}} \in [0.38e^{j0}, 1e^{j2\pi}]. \tag{14}$$

To obtain the range of effective weights possible when the joint effect of the Fermi energies of the modulator and the antenna is considered, an exhaustive data set with all combinations of $EF_{\mathrm{mod}}, EF_{\mathrm{ant}}$ is generated. The effective

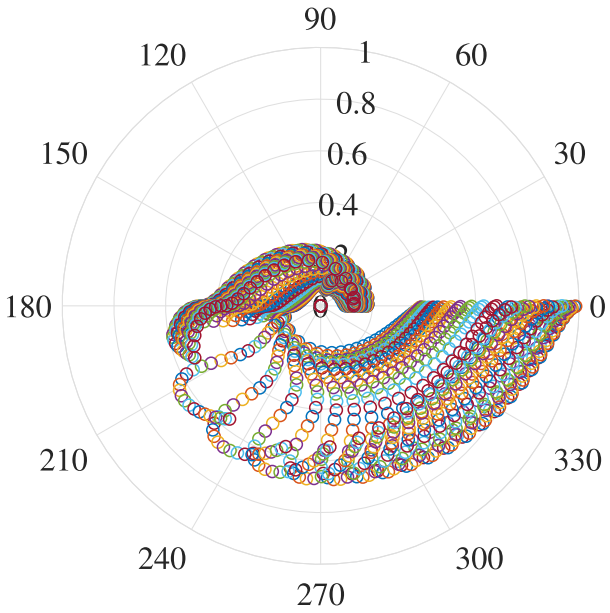

Fig. 8. A polar representation of all effective weights $W_{\mathrm{Joint}_{\mathrm{codebook}}}$ that are implementable in the joint consideration of the codebook design.

weights are analytically calculated for each combination and are displayed in Fig. 8. Every point in Fig. 8 represents an effective weight on the complex plane (radius r represents the signal strength and angle θ represents the phase). Utilizing the data-set presented in Fig. 8, all possible codebooks, C, attainable when we consider phase and amplitude control jointly can then have effective weights $W_{\mathrm{Joint}_{\mathrm{codebook}}}$, given by:

$$W_{\mathrm{Joint}_{\mathrm{codebook}}} \in [0.18e^{j0}, 1e^{j2\pi}]. \tag{15}$$

As discussed in Sec. V, to design the codebook from the joint data set, an algorithm is developed. A simple case to demonstrate the effectiveness of the algorithm is to generate a codebook that, when applied to the array, implements complete phase control at a near constant signal amplitude.

Algorithm Weight Computation Algorithm

Input: Intended Direction (θ_0, ϕ_0), Array Dimensions (NxM)
Output: Weights $\Rightarrow$ As Modulator, Antenna Fermi energy.
W(0,0) = $[EF_{\mathrm{mod}_{0,0}}, Ef_{\mathrm{ant}_{0,0}}] \Leftarrow$ reference weight at origin
W(1,0) = $[EF_{\mathrm{mod}_{1,0}}, Ef_{\mathrm{ant}_{1,0}}] \Leftarrow$ element weight at (1,0)
$\vdots \quad \vdots \quad \vdots$
W(n,m) = $[EF_{\mathrm{mod}_{n,m}} \; Ef_{\mathrm{ant}_{n,m}}] \Leftarrow$ element weight at (n,m)
$\vdots \quad \vdots \quad \vdots$
W(N,M) = $[EF_{\mathrm{mod}_{N,M}} \; Ef_{\mathrm{ant}_{N,M}}] \Leftarrow$ element weight at (N,M) All possible effective weights are: $Ae^{j\beta}$

for All effective weights with β = 0° **do**
  Choose W(0,0) with Max(A)$\Rightarrow [EF_{\mathrm{mod}_{0,0}}, EF_{\mathrm{ant}_{0,0}}]$.
end for
$\beta_x, \beta_y \Leftarrow$ relative phase delay required along x and y direction.
for $m = 0 - M$ **do**

  if $m\beta_y > Q(2\pi)$, where $Q \geq 1$ **then**
    req-delay-y = $m\beta_y - Q(2\pi)$ [account for periodicity]
  else
    req-delay-y= $m\beta_y$
  end if
  Find $W(0, m) = Ae^{j\beta_{0,m}}$ such that $\beta_{0,m}$ = m.req-delay-y
  for $n = 1 - N$ **do**

    if $n\beta_x > Q(2\pi)$, where $Q \geq 1$ **then**
      req-delay-x = $n\beta_x - Q(2\pi)$ [account for periodicity]
    else
      req-delay-x= $n\beta_x$
    end if
    for All effective weights **do**
      Find $W(n, m) = Ae^{j\beta_{n,m}}$ such that $\beta_{n,m}$ = m.req-delay-y + n.req-delay-x Actual weight$\Rightarrow$ $[EF_{\mathrm{mod}_{n,m}}, EF_{\mathrm{ant}_{n,m}}]$
      $\Rightarrow$ If none, choose $W(n, m)$ with least discrepancy in β
      $\Rightarrow$ If multiple, choose $W(n, m)$ with least power discrepancy with W(0,m)
    end for
    For future $\Rightarrow$ store input $\Rightarrow (\theta_0, \phi_0), (NxM)$ and store computed weight $\Rightarrow [EF_{\mathrm{mod}_{n,m}}, EF_{\mathrm{ant}_{n,m}}]$
    Return the weight $\Rightarrow [EF_{\mathrm{mod}_{n,m}}, EF_{\mathrm{ant}_{n,m}}]$
  end for
end for

Thus, the desired codebook to be generated from this algorithm is to be near identical to a universal phased array codebook.

The effective weights as available that may be considered for such a codebook are retrieved by the algorithm and are presented in Fig. 9, again on the complex plane. It is seen that the effective weights indeed meet the criteria for continuous phase control, with the maximum discrepancies in signal strengths of any two effective weights at less than a factor of 2. It is important to note that the digitization of the effective weights and the empty regions seen in Fig. 9 are manifestations of the step-size considered while obtaining the data-set. As discussed in Sec. V, the step-size may be reduced for increased precision, at a higher computational cost.

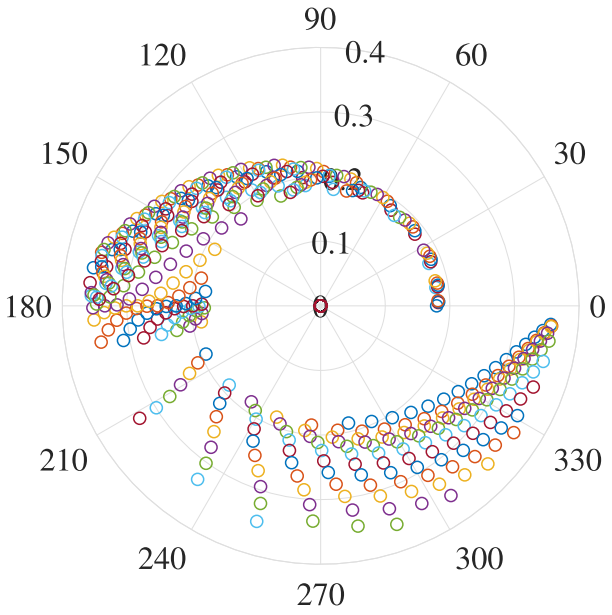

Fig. 9. A polar representation of the effective weights returned by the algorithm for implementation of a universal phased array codebook.

The algorithm is a twofold process: the determination of the criterion for finding the weights, and the mapping of the weights to the Fermi energy of the modulator and the antenna. In the previous case, the progressive phase is determined through (10), with a condition imposed on the maximum amplitude discrepancy to be within a factor of 2. At the same time, the criteria could be reversed to place greater emphasis on matching the signal strengths of all the elements at the cost of a greater deviation in the required phase and actual phase. Similarly, the ability to perform continuous dynamic control on the phase and amplitude could be exploited to perform adaptive beamforming, whereby the radiated power can be simultaneously directed in the intended direction and truncated greatly in other undesirable directions. The method of acquiring the weights in such scenarios are quite complex and thus their analysis is left out of the scope of this work.

Nonetheless, the performance of the algorithm cannot be considered optimal without a strict definition on the metric of optimality, which may change as per the required scenario. However, it is important to note that the data-set over which the algorithm operates is independent of the criterion required for selecting the weights. Thus, the data-set of phase and signal strength for different modulator and antenna Fermi energies is fixed for the array elements. Only an actual change in the physical dimensions of the front-end (such as, for example, physical length, operating frequency, substrate permittivity or thickness) would require the repetition of the numerical analysis for obtaining a new data-set. Therefore, the actual

TABLE II
THE DERIVED CODEBOOKS

Ideal Codebook	Applied Phase at Front-end elements (rad)		
	$W_{0,0}$	$W_{1,0}$	$W_{2,0}$
$C0$	$1e^{j0}$	$1e^{j\pi/2}$	$1e^{j\pi}$

Derived Codebooks	Fermi Energy of Stubs (eV)					
	$EF_{\text{mod}_{0,0}}$	$EF_{\text{ant}_{0,0}}$	$EF_{\text{mod}_{1,0}}$	$EF_{\text{ant}_{1,0}}$	$EF_{\text{mod}_{2,0}}$	$EF_{\text{ant}_{2,0}}$
$C1$	0.16	1.25	0.23	1.25	0.35	1.25
$C2$	0.16	1.2	0.23	1.29	0.35	1.44
$C3$	0.17	1.29	0.24	1.44	0.37	1.01

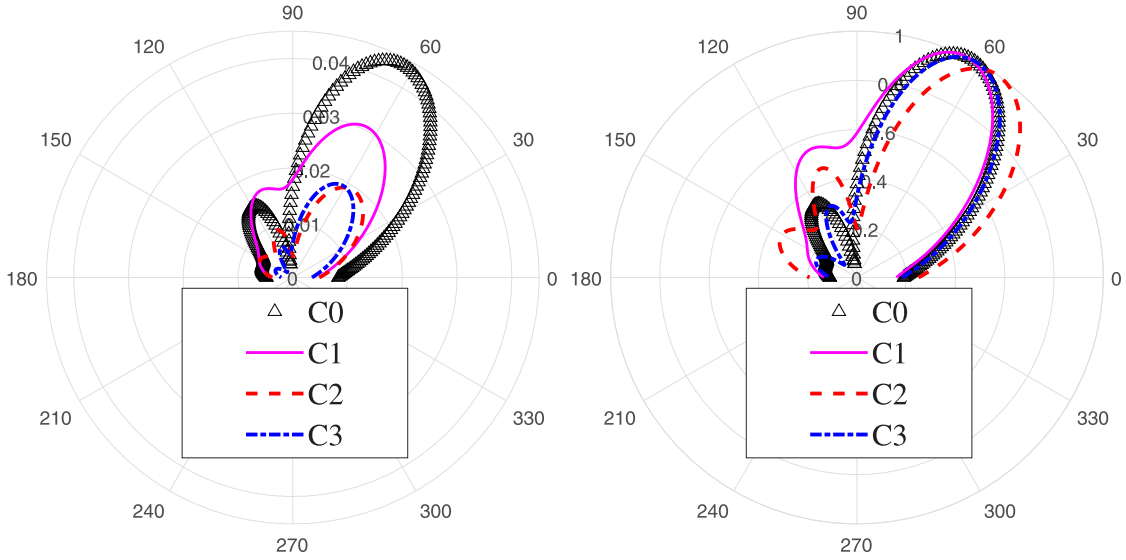

(a) Far-field (b) Normalized Far-field

Fig. 10. a) Far-field radiation patterns obtained from the implementation of the four different codebooks in Table II, intended to steer the beam towards $(\theta_0, \phi_0) = (30°, 0°)$: C0 - Ideal weight, C1 - Phase control, C2 - Independently considered phase and amplitude control, C3 - Jointly considered phase and amplitude control. b) Normalized far-field radiation patterns of the far-field radiation patterns generated.

process of the algorithm for scanning the weights and returning them is near instantaneous.

B. Beamforming Capabilities

1) Codebook Design: To demonstrate the efficiency of the algorithm and benchmark it to that of independent phase and amplitude control, a 3×1 array is designed and its performance is analysed. The codebook C to be implemented at the array is intended to steer the beam at a direction of $30°$ from the broadside (elevation angle of $90°$), or where $(\theta_0, \phi_0) = (30°, 0°)$. From (10), the relative phase delay required between the elements is 1.57 radians. The ideal effective weights for a codebook so designed are then: $W_{0,0} = 1e^{j\cdot0}, W_{0,1} = 1e^{j\cdot\pi/2}, W_{0,2} = 1e^{j\cdot\pi}$. The codebook is implemented through the derived Fermi energies of the modulator and the antenna.

Table II shows the three different codebooks obtained from the cases considered, following the discussion from Sec. V. The ideal codebook $C0$ (a direct implementation of the effective weights at the antenna input port, i.e, bypassing the modulator) is also shown. The codebook $C1$ is derived by considering only phase control. The codebook $C2$ is derived where both phase and amplitude control are considered, albeit independently. The third codebook, $C3$ is obtained through the algorithm, considering the joint relationship between phase and amplitude control. Fig. 10(a) shows the far-field radiation patterns of the array, corresponding to the four different codebooks applied from Table II. When the codebook $C0$ is applied, the far-field radiation pattern of a phased array as per array theory is obtained. When the codebook $C1$ is applied, it is seen that the main-lobe of the far-field pattern is indeed pointed towards the intended direction, along with significant side-lobe strength. The maximum discrepancy in the signal strengths across the different elements is 4.1. The application of codebook $C2$ corresponds to a far-field pattern where it is seen that the side-lobe strength is effectively attenuated, but at the cost of directional accuracy. The far-field radiation pattern that corresponds to the application of the codebook $C3$ exhibits the desired side-lobe attenuation and directional accuracy as per the ideal case.

If the power output of the array in the main, intended direction is of primary concern and is to be maximized, it may be beneficial to perform only phase control as amplitude control attenuates power output. However, when pencil thin

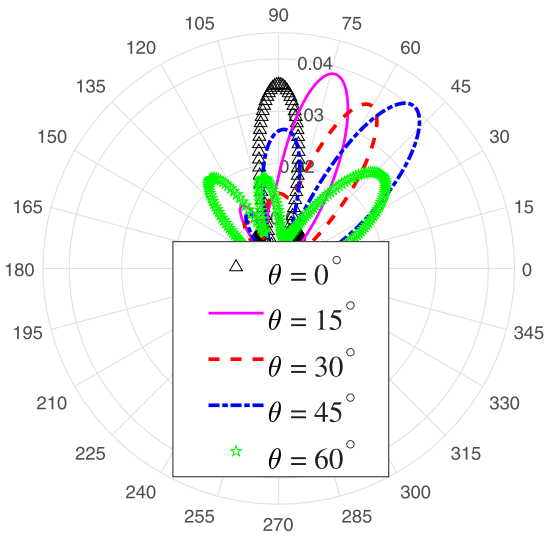

Fig. 11. Far-field radiation patterns of a 6×1 array from the application of codebooks designed for beamsteering at: $(\theta_0, \phi_0) = (0°, 0°), (15°, 0°), (30°, 0°), (45°, 0°)$ *and* $(60°, 0°)$.

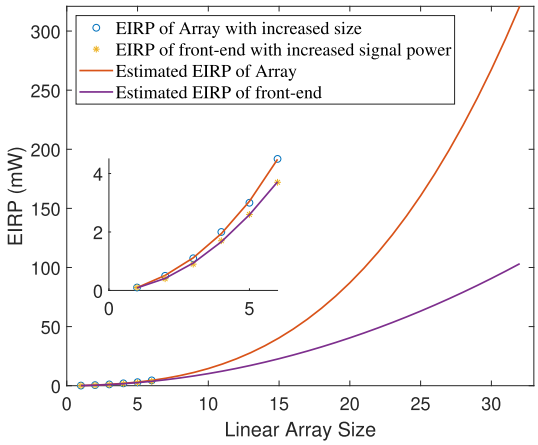

Fig. 12. EIRP as a function of the number of elements.

beams are important, the side-lobe strength must be minimized and both phase and amplitude control are required. In such cases it is necessary to consider the joint effect and proceed with the complex algorithm to generate the codebook.

To highlight the important deviations of these three scenarios, normalized versions of the far-field patterns are shown in Fig. 10(b). The application of codebook $C3$, derived from the algorithm allows superior capability in minimizing side-lobe strength while maintaining directional accuracy; it is the closest imitation of the ideal case. Thus, the consideration of the joint weight definition (13) and the use of computational resources for utilizing the algorithm are justified, as these improve the performance of the array.

2) Dynamic Beamforming Ability: The plasmonic array is designed to have continuous phase control. To examine the limits on beamsteering, the performance of a designed 6 by 1 array is investigated. The codebook required is generated using the algorithm. Since the array facilitates continuous phase delay, any and all intended directions are theoretically possible. However, as mentioned in Sec. IV, the antenna at the front-end is designed as a broadside radiator. Therefore, the further the intended direction of the beam deviates from broadside, the more the limitation of the radiation pattern of the antenna itself becomes visible [51].

Fig. 11 presents the resultant far-field radiation patterns obtained from the implementation of 5 different codebooks, designed to steer a 6×1 array towards $(\theta_0, \phi_0) = (0°, 0°), (15°, 0°), (30°, 0°), (45°, 0°)$ and $(60°, 0°)$. It is seen that the array successfully steers across this broad range of angles, with directional accuracy. There are slight inequalities in the output power of the main-lobes between different directions, as well as non-negligible sidelobes present for intended directions of steering of $(45°, 0°)$ *and* $(60°, 0°)$. These occur both due to the manifestations of the effect of Fermi energies of the modulator and the antenna on signal strengths of the front-ends, as well as the individual radiation pattern of the antenna itself. Since the algorithm allows for a certain discrepancy in the maximum strengths of the antenna elements, the theoretical cancellations of the null points are not absolute. At the same time however, the benefit of continuous beamforming support from the design of the array allows for the possibility of implementing adaptive beamforming algorithms. As discussed in VI-A, these can be utilized, inter alia, to minimize the sidelobe strengths in scenarios where these may be undesirable or unacceptable.

C. Output Power

It is explained in Sec. III that every front-end, or element, in the plasmonic array has an independent source. Therefore, as the size of the designed array increases, the radiation efficiency increases, both due to the addition of more signal sources as well as directional beamforming.

In Fig. 12, the Effective Isotropic Radiated Power (EIRP) of a linear array at different sizes is presented. Additionally, the EIRP of a single front-end where the signal source has the cumulative power of the total no. of array elements is also plotted. Up to a 6×1 array size, the EIRP is obtained through numerical analyses, after which a polynomial extrapolation is performed to obtain the estimated EIRP of a larger array. The same method is followed for the individually considered front-end. As expected, it is seen that the EIRP of the array outperforms the front-end, where the total input power is the same.

For a 6×1 array designed following the guidelines presented in this paper, the EIRP and footprint size are $4.5\,\mathrm{mW}$ and $0.056\,\mathrm{mm}^2$, respectively. Thus, the transmitted power density of a 6×1 plasmonic array is $80.16\,\mathrm{mW/mm}^2$. Using a polynomial approximation, a 32×1 array is estimated to have an EIRP greater than $300\,\mathrm{mW}$. The footprint of the array would be $0.3\,\mathrm{mm}^2$, and the radiation efficiency would be $1000\,\mathrm{mW/mm}^2$.

VII. Discussion

In this section, we discuss the key technical challenges and the opportunities that are present in realizing the design parameters of the plasmonic array architecture.

A. Challenges in Graphene Technology

To perform accurate control of the graphene-based modulator and antenna as required to design the codebook, the use of electrostatic bias places an upper restriction on the maximum attainable Fermi energy. The restriction occurs when the electric field required reaches values that can cause dielectric breakdown of the substrate considered, as highlighted in [57]. However, the maximum value of the Fermi energy can be increased for the same electric bias with a higher Fermi velocity in graphene. As shown in [58], there are several methods to engineer an increased Fermi velocity in graphene through which the restriction on the maximum Fermi energy can be substantially increased. Following such methods, the maximum Fermi energy attainable can be pushed to facilitate the range considered.

Additionally, the effect of power attenuation and the propagation of plasmons along the graphene layer requires a relaxation time greater than that which is achieved from the most common fabrication methods. While the relaxation time considered is certainly possible as highlighted in Sec. IV-C, it requires sophisticated fabrication techniques. A compromise on the quality of graphene fabrication results in a reduced relaxation time [59], with greater power attenuation. Worse, the plasmons may completely die out before traversing the complete length of the front-end, resulting in the front-end being in an "off" state.

B. Realization and Integration of Array Components

The independent integration of the source allows a non-linear increase in the power output of the array architecture, as demonstrated in Sec. VI. However, the independence of each signal source also increases the challenge of proper synchronization. On the one hand, the application of accurate clock control at the transmission side can be used to solve this, albeit at the cost of a more complex hardware setup. On the other hand, the use of smart data synchronization methods directly at the receiver end as in [60] may be considered, for a simpler hardware design at the cost of more complex computational methods.

Along with the benefit of individual control over every element of the array for a multi-functional and vast codebook design, the trade-off is in the realization of local biasing schemes for controlling the graphene patches of the antenna and the modulator for every front end. While a fully functional array design requires the highest level of control, a compromise is possible by considering an array of sub-arrays, with each sub-array controlled as one rather than every individual element. Such schemes have been previously proposed as a way to overcome the high cost, footprint and power consumption of traditional array designs [61], [62]. The practical consideration of the sub-array size, and the trade-off between beamforming control and complexity is clearly a non-trivial task.

VIII. Conclusion

In this paper, we have proposed a plasmonic nano-antenna array architecture and demonstrated that it supports dynamic beamforming with full (phase and amplitude) weight control. By considering the combined effect of the Fermi energy of the modulator and of the antenna in the derivation of the codebook, we have been able to successfully demonstrate dynamic beamforming with accuracy. With the addition of an independent signal source with each element and the ability to define narrow directional beams, the power density of the array increases non-linearly with its size. Due to the dependency of the array design on the plasmonic wavelength, the array that can be designed following this architecture can be compact, with a strong EIRP and versatile beamforming capability. Our future work is aimed at fabricating and experimentally testing the performance of the array.

References

[1] R. Piesiewicz *et al.*, "Short-range ultra-broadband terahertz communications: Concepts and perspectives," *IEEE Antennas Propag. Mag.*, vol. 49, no. 6, pp. 24–39, Dec. 2007.

[2] J. Federici and L. Moeller, "Review of terahertz and subterahertz wireless communications," *J. Appl. Phys.*, vol. 107, no. 11, Jun. 2010, Art. no. 111101.

[3] H.-J. Song and T. Nagatsuma, "Present and future of terahertz communications," *IEEE Trans. THz Sci. Technol.*, vol. 1, no. 1, pp. 256–263, Sep. 2011.

[4] I. F. Akyildiz, J. M. Jornet, and C. Han, "Terahertz band: Next Frontier for wireless communications," *Phys. Commun.*, vol. 12, pp. 16–32, Sep. 2014.

[5] T. S. Rappaport *et al.*, "Wireless communications and applications above 100 GHz: Opportunities and challenges for 6G and beyond," *IEEE Access*, vol. 7, pp. 78729–78757, 2019.

[6] I. F. Akyildiz, C. Han, and S. Nie, "Combating the distance problem in the millimeter wave and terahertz frequency bands," *IEEE Commun. Mag.*, vol. 56, no. 6, pp. 102–108, Jun. 2018.

[7] K. Sengupta, T. Nagatsuma, and D. M. Mittleman, "Terahertz integrated electronic and hybrid electronic–photonic systems," *Nature Electron.*, vol. 1, no. 12, p. 622, Dec. 2018.

[8] A. Nikpaik, A. H. M. Shirazi, A. Nabavi, S. Mirabbasi, and S. Shekhar, "A 219-to-231 GHz frequency-multiplier-based VCO with ~3% peak DC-to-RF efficiency in 65-nm CMOS," *IEEE J. Solid-State Circuits*, vol. 53, no. 2, pp. 389–403, Feb. 2018.

[9] E. Schlecht *et al.*, "Schottky diode based 1.2 THz receivers operating at room-temperature and below for planetary atmospheric sounding," *IEEE Trans. THz Sci. Technol.*, vol. 4, no. 6, pp. 661–669, Nov. 2014.

[10] J. V. Siles, K. B. Cooper, C. Lee, R. H. Lin, G. Chattopadhyay, and I. Mehdi, "A new generation of room-temperature frequency-multiplied sources with up to 10× higher output power in the 160-GHz–1.6-THz range," *IEEE Trans. THz Sci. Technol.*, vol. 8, no. 6, pp. 596–604, Nov. 2018.

[11] T. Nagatsuma, G. Ducournau, and C. C. Renaud, "Advances in terahertz communications accelerated by photonics," *Nature Photon.*, vol. 10, p. 371, May 2016.

[12] Q. Lu, D. Wu, S. Sengupta, S. Slivken, and M. Razeghi, "Room temperature continuous wave, monolithic tunable THz sources based on highly efficient mid-infrared quantum cascade lasers," *Sci. Rep.*, vol. 6, no. 1, Jul. 2016, Art. no. 23595.

[13] *VDI Passive Devices*. Accessed: Sep. 30, 2019. [Online]. Available: https://www.vadiodes.com/en/products/straight-waveguides-tapers-horn-antenna-directional-couplers

[14] *Mi-Wave Antennas*. Accessed: Sep. 30, 2019. [Online]. Available: https://www.miwv.com/millimeter-wave-products/antenna-products/

[15] K. Fan, Z.-C. Hao, Q. Yuan, and W. Hong, "Development of a high gain 325–500 GHz antenna using quasi-planar reflectors," *IEEE Trans. Antennas Propag.*, vol. 65, no. 7, pp. 3384–3391, Jul. 2017.

[16] N. Llombart, G. Chattopadhyay, A. Skalare, and I. Mehdi, "Novel terahertz antenna based on a silicon lens fed by a leaky wave enhanced waveguide," *IEEE Trans. Antennas Propag.*, vol. 59, no. 6, pp. 2160–2168, Jun. 2011.

[17] K. Konstantinidis *et al.*, "Low-THz dielectric lens antenna with integrated waveguide feed," *IEEE Trans. THz Sci. Technol.*, vol. 7, no. 5, pp. 572–581, Sep. 2017.

[18] A. Simsek, S.-K. Kim, and M. J. W. Rodwell, "A 140 GHz MIMO transceiver in 45 nm SOI CMOS," in *Proc. IEEE BiCMOS Compound Semiconductor Integr. Circuits Technol. Symp. (BCICTS)*, Oct. 2018, pp. 231–234.

[19] K. M. Luk *et al.*, "A microfabricated low-profile wideband antenna array for terahertz communications," *Sci. Rep.*, vol. 7, no. 1, Dec. 2017, Art. no. 1268.

[20] C. Lee *et al.*, "Terahertz antenna arrays with silicon micromachined-based microlens antenna and corrugated horns," in *Proc. Int. Workshop Antenna Technol. (iWAT)*, Mar. 2015, pp. 70–73.

[21] E. García-Muñoz *et al.*, "Photonic-based integrated sources and antenna arrays for broadband wireless links in terahertz communications," *Semicond. Sci. Technol.*, vol. 34, no. 5, May 2019, Art. no. 054001.

[22] A. C. Ferrari *et al.*, "Science and technology roadmap for graphene, related two-dimensional crystals, and hybrid systems," *Nanoscale*, vol. 7, no. 11, pp. 4598–4810, Sep. 2015.

[23] P. A. D. Gonçalves and N. M. Peres, *An Introduction to Graphene Plasmonics*. Singapore: World Scientific, 2016.

[24] J. M. Jornet and I. F. Akyildiz, "Graphene-based plasmonic nano-transceiver for terahertz band communication," in *Proc. 8th Eur. Conf. Antennas Propag. (EuCAP)*, Apr. 2014, pp. 492–496.

[25] M. Nafari, G. R. Aizin, and J. M. Jornet, "Plasmonic HEMT terahertz transmitter based on the Dyakonov–Shur instability: Performance analysis and impact of nonideal boundaries," *Phys. Rev. A, Gen. Phys.*, vol. 10, no. 6, Dec. 2018, Art. no. 064025.

[26] B. Sensale-Rodriguez *et al.*, "Broadband graphene terahertz modulators enabled by intraband transitions," *Nature Commun.*, vol. 3, no. 1, p. 780, Jan. 2012.

[27] P. K. Singh, G. Aizin, N. Thawdar, M. Medley, and J. M. Jornet, "Graphene-based plasmonic phase modulator for terahertz-band communication," in *Proc. 10th Eur. Conf. Antennas Propag. (EuCAP)*, Apr. 2016, pp. 1–5.

[28] T.-T. Kim *et al.*, "Amplitude modulation of anomalously refracted terahertz waves with gated-graphene metasurfaces," *Adv. Opt. Mater.*, vol. 6, no. 1, Jan. 2018, Art. no. 1700507.

[29] J. M. Jornet and I. F. Akyildiz, "Graphene-based plasmonic nano-antenna for terahertz band communication in nanonetworks," *IEEE J. Sel. Areas Commun.*, vol. 31, no. 12, pp. 685–694, Dec. 2013.

[30] M. Tamagnone, J. Gomez-Diaz, J. R. Mosig, and J. Perruisseau-Carrier, "Reconfigurable terahertz plasmonic antenna concept using a graphene stack," *Appl. Phys. Lett.*, vol. 101, no. 21, 2012, Art. no. 214102.

[31] I. F. Akyildiz and J. M. Jornet, "Realizing ultra-massive MIMO (1024×1024) communication in the (0.06–10) terahertz band," *Nano Commun. Netw.*, vol. 8, pp. 46–54, Jun. 2016.

[32] C. Lin and G. Y. Li, "Indoor terahertz communications: How many antenna arrays are needed?" *IEEE Trans. Wireless Commun.*, vol. 14, no. 6, pp. 3097–3107, Jun. 2015.

[33] X. Mei *et al.*, "First demonstration of amplification at 1 THz using 25-nm InP high electron mobility transistor process," *IEEE Electron Device Lett.*, vol. 36, no. 4, pp. 327–329, Apr. 2015.

[34] K. Vijayraghavan *et al.*, "Broadly tunable terahertz generation in mid-infrared quantum cascade lasers," *Nature Commun.*, vol. 4, no. 1, p. 2021, Oct. 2013.

[35] Y. Luo *et al.*, "A graphene-based tunable negative refractive index metamaterial and its application in dynamic beam-tilting terahertz antenna," *Microw. Opt. Technol. Lett.*, vol. 61, no. 12, pp. 2766–2772, Dec. 2019.

[36] S. E. Hosseininejad, K. Rouhi, M. Neshat, A. Cabellos-Aparicio, S. Abadal, and E. Alarcon, "Digital metasurface based on graphene: An application to beam steering in terahertz plasmonic antennas," *IEEE Trans. Nanotechnol.*, vol. 18, pp. 734–746, 2019.

[37] P.-Y. Chen, C. Argyropoulos, and A. Alu, "Terahertz antenna phase shifters using integrally-gated graphene transmission-lines," *IEEE Trans. Antennas Propag.*, vol. 61, no. 4, pp. 1528–1537, Apr. 2013.

[38] P.-Y. Chen and A. Alù, "THz beamforming using graphene-based devices," in *Proc. IEEE Radio Wireless Symp.*, Jan. 2013, pp. 55–57.

[39] M. Dyakonov and M. Shur, "Shallow water analogy for a ballistic field effect transistor: New mechanism of plasma wave generation by DC current," *Phys. Rev. Lett.*, vol. 71, no. 15, p. 2465, 1993.

[40] T. Otsuji, Y. M. Meziani, M. Hanabe, T. Ishibashi, T. Uno, and E. Sano, "Grating-bicoupled plasmon-resonant terahertz emitter fabricated with GaAs-based heterostructure material systems," *Appl. Phys. Lett.*, vol. 89, no. 26, Dec. 2006, Art. no. 263502.

[41] T. Otsuji, V. Popov, and V. Ryzhii, "Active graphene plasmonics for terahertz device applications," *J. Phys. D, Appl. Phys.*, vol. 47, no. 9, Mar. 2014, Art. no. 094006.

[42] Y.-J. Yu, Y. Zhao, S. Ryu, L. E. Brus, K. S. Kim, and P. Kim, "Tuning the graphene work function by electric field effect," *Nano Lett.*, vol. 9, no. 10, pp. 3430–3434, Oct. 2009.

[43] G. W. Hanson, "Dyadic Green's functions and guided surface waves for a surface conductivity model of graphene," *J. Appl. Phys.*, vol. 103, no. 6, Mar. 2008, Art. no. 064302.

[44] L. A. Falkovsky and A. A. Varlamov, "Space-time dispersion of graphene conductivity," *Eur. Phys. J. B*, vol. 56, no. 4, pp. 281–284, Apr. 2007.

[45] G. W. Hanson, "Dyadic Green's functions for an anisotropic, non-local model of biased graphene," *IEEE Trans. Antennas Propag.*, vol. 56, no. 3, pp. 747–757, Mar. 2008.

[46] M. Nafari and J. M. Jornet, "Modeling and performance analysis of metallic plasmonic nano-antennas for wireless optical communication in nanonetworks," *IEEE Access*, vol. 5, pp. 6389–6398, 2017.

[47] P. Berini, "Figures of merit for surface plasmon waveguides," *Opt. Express*, vol. 14, no. 26, pp. 13030–13042, 2006.

[48] M. Andrello, A. Singh, N. Thawdar, and J. M. Jornet, "Dynamic beamforming algorithms for ultra-directional terahertz communication systems based on graphene-based plasmonic nano-antenna arrays," in *Proc. 52nd Asilomar Conf. Signals, Syst., Comput.*, Oct. 2018, pp. 1558–1563.

[49] D. R. Jackson, C. Caloz, and T. Itoh, "Leaky-wave antennas," *Proc. IEEE*, vol. 100, no. 7, pp. 2194–2206, Jul. 2012.

[50] M. Esquius-Morote, J. S. Gomez-Diaz, and J. Perruisseau-Carrier, "Sinusoidally modulated graphene leaky-wave antenna for electronic beamscanning at THz," *IEEE Trans. THz Sci. Technol.*, vol. 4, no. 1, pp. 116–122, Jan. 2014.

[51] C. A. Balanis, *Antenna Theory: Analysis and Design*. Hoboken, NJ, USA: Wiley, 2016.

[52] C. R. Dean *et al.*, "Boron nitride substrates for high-quality graphene electronics," *Nature Nanotechnol.*, vol. 5, no. 10, p. 722, 2010.

[53] L. Banszerus *et al.*, "Ultrahigh-mobility graphene devices from chemical vapor deposition on reusable copper," *Sci. Adv.*, vol. 1, no. 6, Jul. 2015, Art. no. e1500222.

[54] L. Banszerus *et al.*, "Extraordinary high room-temperature carrier mobility in graphene-WSe_2 heterostructures," 2019, *arXiv:1909.09523*. [Online]. Available: http://arxiv.org/abs/1909.09523

[55] L. Zakrajsek, E. Einarsson, N. Thawdar, M. Medley, and J. M. Jornet, "Design of graphene-based plasmonic nano-antenna arrays in the presence of mutual coupling," in *Proc. 11th Eur. Conf. Antennas Propag. (EUCAP)*, Mar. 2017, pp. 1381–1385.

[56] S. K. Saha *et al.*, "X60: A programmable testbed for wideband 60 GHz wlans with phased arrays," in *Proc. 11th Workshop Wireless Netw. Testbeds, Exp. Eval. CHaracterization (WiNTECH)*, New York, NY, USA, 2017, pp. 75–82.

[57] W. Fuscaldo, P. Burghignoli, P. Baccarelli, and A. Galli, "Graphene Fabry–Pérot cavity leaky-wave antennas: Plasmonic versus nonplasmonic solutions," *IEEE Trans. Antennas Propag.*, vol. 65, no. 4, pp. 1651–1660, Apr. 2017.

[58] C. Hwang *et al.*, "Fermi velocity engineering in graphene by substrate modification," *Sci. Rep.*, vol. 2, no. 1, Dec. 2012, Art. no. 590.

[59] J. S. Gomez-Diaz *et al.*, "Self-biased reconfigurable graphene stacks for terahertz plasmonics," *Nature Commun.*, vol. 6, no. 1, p. 6334, May 2015.

[60] N. BniLam, J. Steckel, and M. Weyn, "Synchronization of multiple independent subarray antennas: An application for angle of arrival estimation," *IEEE Trans. Antennas Propag.*, vol. 67, no. 2, pp. 1223–1232, Feb. 2019.

[61] C. Han, J. M. Jornet, and I. Akyildiz, "Ultra-massive MIMO channel modeling for graphene-enabled terahertz-band communications," in *Proc. IEEE 87th Veh. Technol. Conf. (VTC Spring)*, Jun. 2018, pp. 1–5.

[62] H. Sarieddeen, M.-S. Alouini, and T. Y. Al-Naffouri, "Terahertz-band ultra-massive spatial modulation MIMO," 2019, *arXiv:1905.04732*. [Online]. Available: http://arxiv.org/abs/1905.04732

Arjun Singh (Graduate Student Member, IEEE) received the B.S. degree *(summa cum laude)* in electrical engineering and the M.S. degree in electrical engineering from the University at Buffalo-The State University of New York, NY, USA, in 2016 and 2018, respectively. He is currently pursuing the Ph.D. degree under the guidance of Dr. J. M. Jornet. He is a member of the Ultra-Broadband Nanonetworking Laboratory, Northeastern University. His research interests include realizing Terahertz-band wireless communications, graphene-plasmonics, antenna array design, adaptive beamforming, and signal processing.

Michael Andrello III (Student Member, IEEE) received the B.S. degree in materials science and engineering from the Virginia Polytechnic Institute State University, in 2017, and the M.S. degree in electrical engineering from SUNY University at Buffalo in 2019. He is currently a Materials Engineer with Air Force Research Laboratory. His research interests are in the areas of graphene-based plasmonics, antenna design, beamforming arrays, and terahertz band wireless communications.

Ngwe Thawdar (Member, IEEE) received the B.Sc. degree in electrical engineering from The State University of New York and Binghamton University in 2009, and the M.Sc. and Ph.D. degrees in electrical engineering from the University at Buffalo-The State University of New York, in 2011 and 2018, respectively. She has been with the Air Force Research Laboratory Information Directorate, Rome, NY, USA, since 2012. She is currently serving as a Technical Lead of the AFRL's Terahertz Communications Portfolio. Her research interests include wireless spread spectrum communications, software-defined radio implementation, and communications and networking in emerging spectral bands, such as mm-waves and terahertz band frequencies.

Josep Miquel Jornet (Member, IEEE) received the B.S. degree in telecommunication engineering and the M.Sc. degree in information and communication technologies from the Universitat Politècnica de Catalunya, Barcelona, Spain, in 2008, and the Ph.D. degree in electrical and computer engineering from the Georgia Institute of Technology (Georgia Tech), Atlanta, GA, USA, in 2013. From September 2007 to December 2008, he was a Visiting Researcher with the Massachusetts Institute of Technology (MIT), Cambridge, under the MIT Sea Grant Program. From August 2013 and August 2019, he was a Faculty Member with the Department of Electrical Engineering, University at Buffalo-The State University of New York. Since August 2019, he has been an Associate Professor with the Department of Electrical and Computer Engineering, Northeastern University, Boston, MA, USA. His current research interests are in Terahertz-band communication networks, wireless nano-bio-communication networks and the Internet of Nano-Things. In these areas, he has coauthored more than 120 peer-reviewed scientific publications and one book. He has been granted three U.S. patents. He serves as the lead PI on multiple grants from U.S. federal agencies including the National Science Foundation, the Air Force Office of Scientific Research, and Air Force Research Laboratory. He was a recipient of the National Science Foundation CAREER Award and several other awards from IEEE, ACM, and UB. Since July 2016, he has been the Editor-in-Chief of the *Nano Communication Networks* (Elsevier) Journal.